CHEMISTRY

Molecular insights on confined water in the nanochannels of self-assembled ionic liquid crystal

Yoshiki Ishii[1,2]*, Nobuyuki Matubayasi[3,2], Go Watanabe[4], Takashi Kato[5]*, Hitoshi Washizu[1,2]*

Self-assembled ionic liquid crystals can transport water and ions via the periodic nanochannels, and these materials are promising candidates as water treatment membranes. Molecular insights on the water transport process are, however, less investigated because of computational difficulties of ionic soft matters and the self-assembly. Here we report specific behavior of water molecules in the nanochannels by using the self-consistent modeling combining density functional theory and molecular dynamics and the large-scale molecular dynamics calculation. The simulations clearly provide the one-dimensional (1D) and 3D-interconnected nanochannels of self-assembled columnar and bicontinuous structures, respectively, with the precise mesoscale order observed by x-ray diffraction measurement. Water molecules are then confined inside the nanochannels with the formation of hydrogen bonding network. The quantitative analyses of free energetics and anisotropic diffusivity reveal that, the mesoscale geometry of 1D nanodomain profits the nature of water transport via advantages of dissolution and diffusion mechanisms inside the ionic nanochannels.

INTRODUCTION

Ionic liquid crystals (ILC) form a self-assembled nanostructure with the two moieties of hydrophilic ionic groups and hydrophobic alkyl chains (*1*–*3*). Their nanophases provide different properties related to their own molecular groups. The hydrophilic domain of ionic moieties works as a nanochannel to transport charges and molecules, and structural patterns of the ionic nanochannel can be designed as the various geometries of one-dimensional (1D) columnar, 2D smectic, and 3D bicontinuous phases (*1*–*7*). The liquid-crystalline (LC) assemblies of hydrophobic moieties enable to block the permeation of molecules without any paths of the nanochannels. Experimental techniques for the nanochannel organization and interconnection are widely investigated to control molecular behavior. The hydrophobic domain can be fixed by using the photochemical reaction with polymerizable groups (*1*, *8*, *9*). Recently, suitability of nanostructured ILC polymers to water treatment membrane has been reported (*10*–*15*).

In the past two decades, Kato and co-workers (*1*, *7*–*9*, *11*, *13*–*19*) studied the transport properties of charges and molecules and the macroscopic effects of self-assembled nanostructures over various ILCs and their polymers. The observed ionic conductivities are of the orders of 10^{-7} to 10^{-4} S/cm, and the 3D bicontinuous state is remarkably feasible from the viewpoint of the efficient ion conduction and the fabrication process (*17*–*19*). On the other hand, the 1D columnar state also attracts attentions because of the anisotropic features of transport properties (*13*). The thermotropic ILC of benzyltriethylammonium-based cation and tetrafluoroborate BF_4 anion forms the bicontinuous cubic phase at room temperature (*11*, *18*), and the hexagonal columnar phase exhibits by replacing ethyl groups of the ionic moieties with methyl groups (*13*). The ionic nanochannels enable the material to transport water and charged molecules, such as alkali and alkaline earth metals, fluorides, and SO_4^{2-} (*11*, *13*). In addition, the neutral molecules of glucose, sucrose, and raffinose were also observed to permeate through the nanochannel (*13*).

In the ionic nanochannels, the permeation rates of charged molecules do not correlate with any ionic and hydrated radii (*11*). This selective permeation of ionic species is a fascinating property for the practical usage such as reverse osmotic membrane. However, molecular insights on the transport properties of water and ions remain poorly understood. Here, we remark ILCs as derivatives of room-temperature ionic liquids (*7*, *20*). Water solvation mechanism in ionic liquid is recently reported to be energetically advantageous with respect to the cavity formation in solution (*21*, *22*). The comprehensive experiments with x-ray and neutron diffraction and nuclear magnetic resonance measurements advocated the presence of water-dissolution pocket (*23*, *24*). Confined water molecules then move faster than the cations and anions of ionic liquids, and as observed in the recent experiment of Shimizu *et al.* (*25*), the relative mobility of water molecules reduces by increasing the water concentration. A next important issue is thereby the molecular features of water and ionic molecules in electrolyte solutions.

Molecular dynamics (MD) method is a powerful tool for finding molecular insights on nanoconfined environments in condensed matter. Water molecules confined in the nanochannels of carbon nanotube (CNT) and Nafion have been particularly investigated well via computational approaches (*26*–*31*). The confined water molecules interact and diffuse inside the CNT nanotube and pure water (*26*, *27*). Meanwhile, in the nanoconfined ionic environments, the counterion condensation complicates the transport phenomena of water and ions from the viewpoint of polyelectrolytes (*32*, *33*). The charged CNT nanochannel easily fills with water molecules (*26*), while the mobilities of water molecules were then observed to slow down inside the charged nanochannels (*34*).

---

[1] Graduate School of Information Science, University of Hyogo, 7-1-28 Minatojima-Minamimachi, Chuo-ku, Kobe, Hyogo 650-0047, Japan. [2] Elements Strategy Initiative for Catalysts and Batteries, Kyoto University, Katsura, Kyoto 615-8520, Japan. [3] Division of Chemical Engineering, Graduate School of Engineering Science, Osaka University, Toyonaka, Osaka 560-8531, Japan. [4] Department of Physics, School of Science, Kitasato University, Sagamihara, Kanagawa 252-0373, Japan. [5] Department of Chemistry and Biotechnology, School of Engineering, The University of Tokyo, Bunkyo-ku, Tokyo 113-8656, Japan.

*Corresponding author. Email: y.ishii@sim.u-hyogo.ac.jp (Y.I.); kato@chiral.t.u-tokyo.ac.jp (T.K.); h@washizu.org (H.W.)

Then, let us move on to the case of ILC nanochannels. Nada *et al.* (*35*) computed the diffusivity and stability of water and ions inside the subnanochannel divided from thermotropic ILC. Shirts and co-workers (*36*–*38*) recently reported the molecular transport mechanism of water and organic solutes inside the 1D nanochannel of the columnar nanostructures of lyotropic ILC. The formation of smectic structure of ILCs was also computationally demonstrated in the order of hundred nanoseconds (*39*–*41*). Meanwhile, the self-assembled bicontinuous media are poorly investigated because of the geometrical difficulty of 3D-interconnected nanochannel network. The construction of molecular force fields also remains challenging for room-temperature ionic liquids because of the many-body effects of polarization and charge transfer in condensed phase (*42*–*49*). Although MD simulations enable to observe structural ordering of nonionic LC molecules and self-assembled nanostructures of amphiphilic compounds (*39*, *50*–*55*), the addition of ionic moieties requires further large system and long relaxation time for an MD simulation (*39*–*41*). These issues may be more amplified in thermotropic ILC compounds. As a solution for overcoming these computational difficulties, we recently established the self-consistent modeling scheme combining MD and first-principles calculations based on linear-scaling density functional theory (DFT) (*49*). The self-consistent scheme enables us to refine the atomic charges of molecules theoretically incorporating effective interactions in condensed phase and to revisit the fluidity of ionic liquids by adjusting the effective charges without any references to experimental measurements. As demonstrated for various ionic liquids (*47*–*49*), this approach systematically improves the computational accuracy of the structural, energetic, and transport properties of electrolytes. The potential of mean force and the corresponding binding free energy of cation and anion well follow the computational results using first-principles calculation (*43*), and the heat of vaporization, ionic conductivity, and viscosity also agree with the experimental values.

Here we report specific behavior of water molecules confined in the ILC nanochannels of compound **1** shown in Fig. 1A with all-atom MD simulation. Atomic charge distributions of molecules were determined with the periodic subnanochannels by using a linear-scaling DFT calculation, and a molecular force field for the ILC was then constructed in condensed phase via the self-consistent modeling scheme of MD and DFT methods. To investigate the nature of confined water inside the ionic nanochannel network, we simulated the self-assembled bicontinuous and columnar structures of compound **1** with the advanced force field and discussed the structural, energetic, and transport properties of water and ionic molecules confined in the ionic nanochannels relevant to the ILC polymer suggested as a reverse osmotic membrane (*11*, *13*). In this study, we mainly use TIP3P model as a standard reference to compare quantitative perspectives of confined water in the CNT, Nafion, and ILC nanochannels shown in previous reports (*26*, *27*, *30*, *37*). Furthermore, we demonstrate the universality of qualitative properties of water molecules inside the ILC nanochannels using TIP4P/2005 model (*56*). From an experimental point of view, most water molecules evaporate in the synthesis of thermotropic ILC states, and they can saturate the ILC nanochannels after making the interface with an aqueous solution. On the other hand, in this study, we prepared water molecules in compound **1** from the beginning of an MD simulation. Some water molecules may be observed in the self-assembled LC domains of hydrophobic moieties. Nevertheless, the simulations correspond well to the experimental conditions when the water distribution is relaxed. This computational protocol thereby helps us to investigate statistical properties and their thermodynamic relationship in the ILC nanochannels.

RESULTS

Self-consistent modeling with DFT calculation in condensed phase

We first discuss atomic charge analyses by the DFT calculation of ILC compound **1**. Note that the atomic charges of anion and cation were determined for the subnanochannel, not including any water molecules as depicted in Fig. 1C, under the periodic boundary condition. In the self-consistent scheme, we rely on a manner of the optimized potentials of liquid simulations (OPLS) with all-atom model as the reference force field (*42*, *57*–*60*). Figure 1D shows the convergence of DFT-based molecular charges and the charge distributions of anion, cation, and atomic groups within the cation of compound **1**. The total charges of cation and anion are calculated by averaging the DFT charges of 200 snapshot configurations. In the self-consistent scheme, as observed in previous studies (*47*–*49*), the first iteration step provides an overshoot value for the molecular charge, and it well converges after the second iteration step. Here, since the calculated density, radial distribution function, and self-diffusion coefficients of molecules are converged within four iterations as demonstrated in the previous study (fig. S1), the self-consistent scheme is finalized at the fourth iteration step. The molecular charge of compound **1** yields ±0.831 on the average at the final iteration step, and the partial charge of ammonium group is +0.648 (table S1). The charge transfer occurs mainly between the ammonium group and BF_4 anion, which shifts the charge distribution of the hydrophobic moiety toward the cationic region as shown in Fig. 1E. In condensed phase, the effects of charge transfer and intramolecular polarization largely fluctuate the molecular charge of cation because of the presence of 3,4,5-trialkylbenzyl group (fig. S2). Meanwhile, the trends of condensed effect are reasonable as following the reference data of room-temperature ionic liquids (*49*). The molecular force field determined by the self-consistent scheme is named OPLS-DFT here, and the MD results are mentioned hereafter.

Self-assembled nanostructures of ILC

Here, we focus on mesoscale structures of compound **1** with large-scale MD simulations beyond the subnanochannels. Two types of MD simulations were carried out in this study through the different protocols of initial configuration and its equilibration: An MD system for bicontinuous structure was simulated in the isothermal-isobaric (*NPT*) ensemble with disordered random configurations and the annealing procedure from 500 K, and the other system for columnar structure was treated in the *NPT* with ordered configurations transformed from the subnanochannel and the careful equilibration at room temperature. See Materials and Methods for the further detailed description. The mole fraction of water molecule, x_w, is set to the range of 0.00 to 0.75 with TIP3P or TIP4P/2005 model. Figure 2 (A to F) shows the snapshots given by the MD calculations of compound **1** at $x_w = 0.50$. The simulations can provide the 1D and 3D nanodomains of the self-assembled columnar and bicontinuous structures, respectively, as observed by x-ray diffraction measurement (*13*, *18*), regardless of water concentration and molecular models (figs. S3 to S8). Figure 2C then shows the gyroid-like 3D

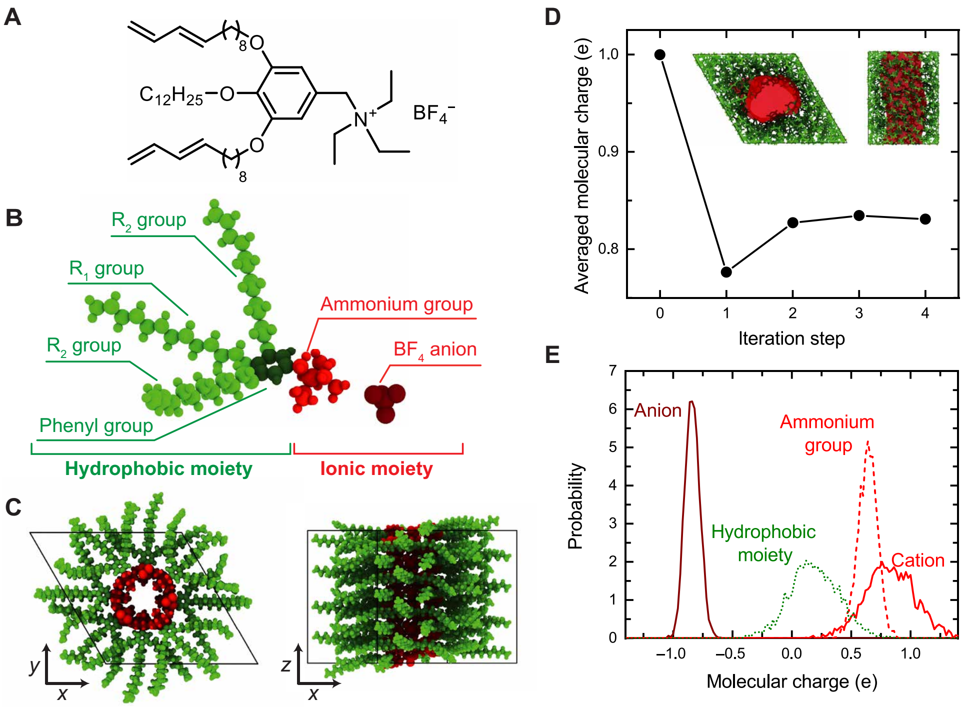

Fig. 1. Molecular information of ILC and the charge distribution obtained by DFT calculation. (**A**) Molecular structure and (**B**) the 3D snapshot of compound **1** and (**C**) the initial configuration of the periodic subnanochannel. (**D**) Convergence of the molecular charges in the self-consistent scheme with MD and DFT methods and (**E**) the charge distributions of anion, cation, and atomic groups within the cation at the final iteration step. The construction protocol of the subnanochannel is described in Materials and Methods. The insets in (D) show the snapshots of the periodic subnanochannel of compound **1**, which are obtained with MD calculation and used in DFT calculation. See fig. S1 for the convergences of calculated density, radial distribution functions, and self-diffusion coefficients through the self-consistent scheme.

nanochannel network with the ionic moieties of ammonium groups and BF_4 anions. More specifically, all the nanodomains of ionic moieties are continuously interconnected under the periodic boundary condition, so that the structural characteristics of bicontinuous motif are simulated in our simulation (fig. S9). Note that the bicontinuous structure was observed at each of five runs with independent initial configurations; see the next paragraph for the detailed mesoscale structures. The annealing simulation from 500 K for 250 ns effectively forms the 3D-interconnected nanochannel network: The number of 3D nanodomains converges to unity by reducing temperature from the counting method of nanodomains (fig. S10). We further remark that the formation of bicontinuous structure can be reproduced even through the annealing procedure from 700 K and the long time relaxation of 500 ns as following the previous reports of smectic ILC structure (*40*, *41*). In contrast, Fig. 2 (E and F) shows the columnar structure with 1D ionic nanochannels in the *xy* plane. The number of 1D nanodomains is then found to be 12 by the same counting method with bicontinuous structure (fig. S9). The averaged distances across ionic nanochannels shown in Fig. 2F are 3.70 to 3.84 nm in correspondence to c_w. The system densities of bicontinuous and columnar structures obtained by MD calculations of compound **1** are shown in fig. S11. The volume of an MD system increases by the addition of water molecules, and the molar concentration of water c_w yields 3.32 M at $x_w = 0.75$. Meanwhile, the density changes are small in both the mesoscale structures in comparison with those estimated additively from the densities of the pure systems of ILC and water. This indicates that the free volume of a water molecule is larger in the ILC than in pure water. Here, the columnar structure gives a higher density systematically than the bicontinuous one, while the difference remains quite small by less than 0.2%. The mesoscale structures are thereby found to weakly affect the system density of compound **1**.

Figure 2 (G to L) shows the x-ray weighted structure factor and the spatial density profile of water molecules in compound **1**. In the bicontinuous structure, the first sharp diffraction peak (FSDP) of structure factor is observed to be shifted toward the low-*k* region from 2.0 nm^{-1} ($c_w = 0.00$ M) to 1.6 nm^{-1} ($c_w = 3.32$ M). Water molecules are then delocalized in the *xy* plane depicted in Fig. 2 (C and H) with slight aggregation observed at high c_w. Here, we remark that, although the experimental observation by x-ray diffraction measurement shows the presence of cubic bicontinuous LC structure with perfect symmetry (*18*), the mesoscale structure obtained by the MD simulation reflects only the diffraction pattern of (100) seen in the FSDP of Fig. 2G. This result implies that the mesoscale geometry slightly differs from the cubic bicontinuous LC structure. As a practical problem, the MD simulation of thermotropic LC compounds could face a difficulty associated with the annealing procedure as well known in glassy compounds. Nevertheless, it is noted that the FSDP position k_{FSDP} well agrees with the experimental value of 1.89 nm^{-1} in pure compound **1** reported by Kato and co-workers (*18*). A long annealing procedure might enhance the mesoscale bicontinuous structure with a ~3% variation of k_{FSDP} (fig. S10). However, our MD simulation shows that the 3D-interconnected bicontinuous structure of hydrophobic and hydrophilic domains is found to be observed even with the randomly distributed initial structures. The obtained bicontinuous structures

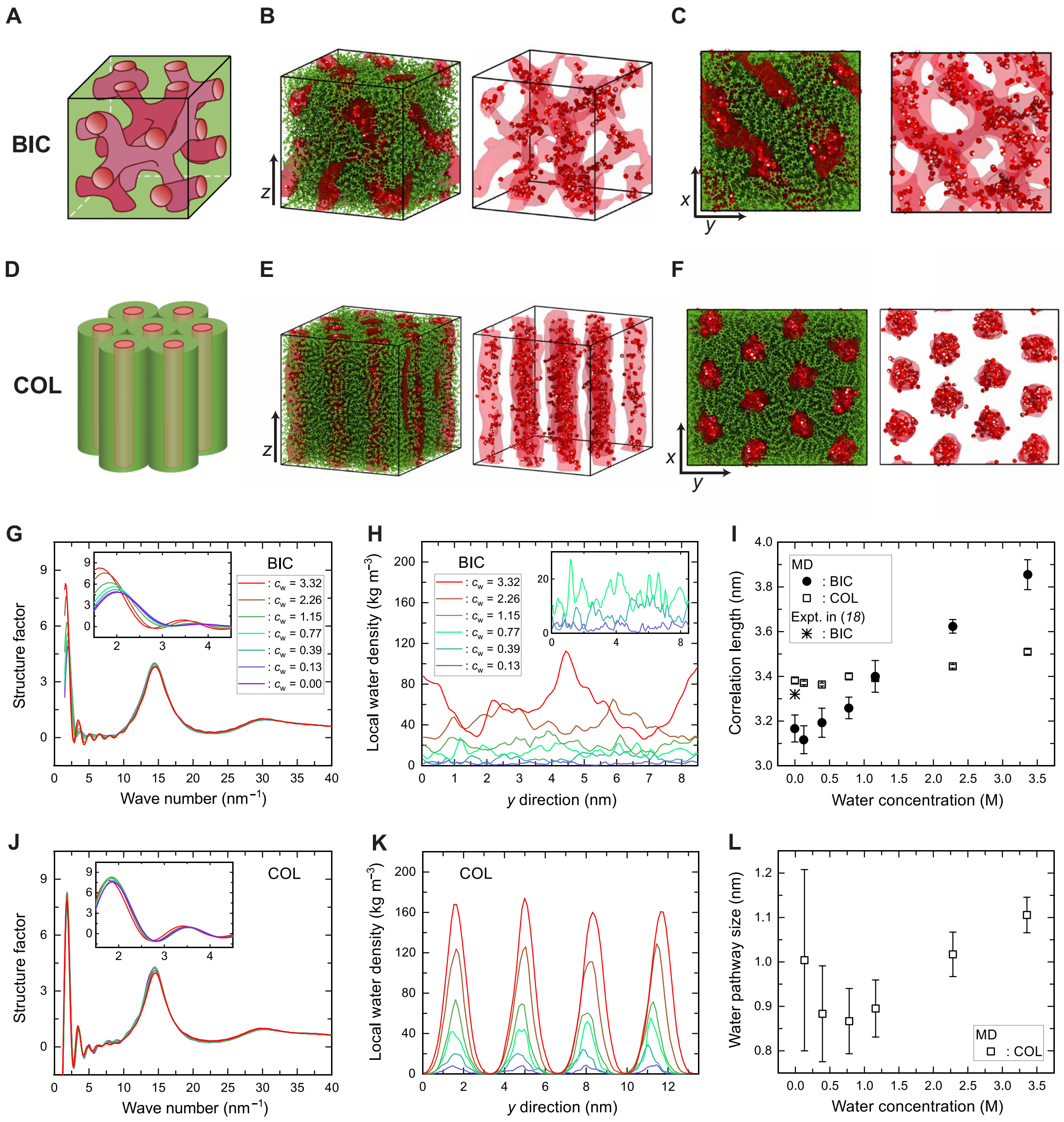

Fig. 2. Snapshots of the nanostructured self-assemblies and their quantitative information obtained by MD calculation with OPLS-DFT and TIP3P. (**A** and **D**) Illustrations of self-assembled bicontinuous and columnar LC structures, respectively, suggested by the experimental observations (*13*, *18*), and (**B**, **C**, **E**, and **F**) the 3D structures of compound **1** at $x_w = 0.50$. The snapshots of (B), (C), (E), and (F) are obtained in the bicontinuous and columnar structures, respectively. BIC and COL represent the obtained data in bicontinuous and columnar structures, respectively. The MD cells are shown with the 3D standpoint along the *z* axis in (B) and (E) and with the 2D standpoint along the perpendicular *xy* plane in (C) and (F). The hydrophilic domains are displayed with the continuum surface (in red) obtained by the spatial distribution of ionic moieties and water molecules. The hydrophobic moieties are depicted with simple bonds (in green) in the left snapshots of (B), (C), (E), and (F), and they are removed in the right ones. All the snapshots are visualized by using OVITO (*70*). (**G** and **J**) X-ray weighted total structure factor and (**H** and **K**) spatial density profile of water molecules. The plots in (G), (H), (J), and (K) are computed in the bicontinuous and columnar structures, respectively. The spatial density profiles in (H) and (K) are calculated along the *y* axis in (C) and (F). (**I**) Correlation lengths and (**L**) water pathway sizes defined by the FSDP of total structure factor and the partial density profile of water molecules, respectively. The correlation length is calculated with the relationship of $L_{\mathrm{FSDP}} = 2\pi/k_{\mathrm{FSDP}}$, and the diameter of water pathway is determined with the half width of fitted Gaussian functions. The error bars of (I) and (L) are shown with twice the SEs (at 95% confidence interval). See fig. S12 for the results with OPLS-DFT and TIP4P/2005.

then enable us to discuss the specific behavior of water confined in the ILC nanochannels.

Figure 2I shows the correlation length defined with the FSDP position as $L_{\mathrm{FSDP}} = 2\pi/k_{\mathrm{FSDP}}$. Since the FSDP arises from the partial structure factor of BF_4-BF_4 (figs. S13 and S14), the correlation length reflects the size of self-assembly formed by hydrophobic moieties of compound **1**. Thereby, as observed in the FSDP of bicontinuous structure, the addition of water molecules results in an increase of the structural scale of self-assembly. In the columnar structure, the structure factor remains unchanged by the addition of water molecules, and the correlation length of FSDP is 3.4 to 3.5 nm in correspondence to the distance between water pathways of 3.7 to 3.8 nm calculated from the equilibrium box size (table S2). Water molecules are then observed to localize in the *xy* plane depicted in Fig. 2F. Here, we analyze the diameter of water pathway via the fitting procedure with Gaussian functions for the spatial density profile of Fig. 2K. The pathway size is roughly 0.90 nm at the low-c_w region, which is comparable to the estimated size of 0.6 nm by the positron-annihilation lifetime spectroscopy (*11*). The addition of water molecules further enlarges the water pathway up to 1.1 nm. This trend of water pathway size corresponds with the computational result in the columnar structure of a lyotropic ILC by Shirts and co-worker (*37*). The same approach is difficult for the bicontinuous structure, since the spatial distribution of the 3D-interconnected nanochannel is different from the isolated one of unidirectional nanochannels formed in the columnar structure. Meanwhile, we can consider that the averaged size of water pathway in the columnar structure agrees with that in the bicontinuous one because of the small difference of system density (fig. S11). Thereby, we summarize here that both of the obtained bicontinuous and columnar structures of compound **1** well satisfy the experimental features of intermediate-range ordering determined by the FSDP of x-ray structure factor and pore diameter estimated experimentally in the well-ordered cubic bicontinuous LC phase by the positron-annihilation lifetime spectroscopy. Here, it is noted that physical properties of confined water essentially depends on short-range structures inside the ILC nanochannels. Therefore, from the next section, we discuss the structural, energetic, and transport properties of water and ions in the bicontinuous and columnar structures of compound **1**.

Structural properties inside the ionic nanochannel

As a first step to understand the energetic and transport properties of ions and water, short-range structures inside the nanochannels are mentioned here with the analysis of radial distribution function shown in Fig. 3. Figure 3 (A to C) shows the radial distribution functions g(r) and potentials of mean force $w(r)$ given by the ionic moieties of ammonium group and BF_4 anion. In this study, $w(r)$ is evaluated with the statistical-mechanical relationship of $-RT\ln g(r)$, and the binding free energy between tagged molecules is defined with the first minimum of $w(r)$. The reference position is set to the center of mass of a targeted group. We can observe the contact ion pair of unlike ions at the equilibrium position of 0.5 nm with the

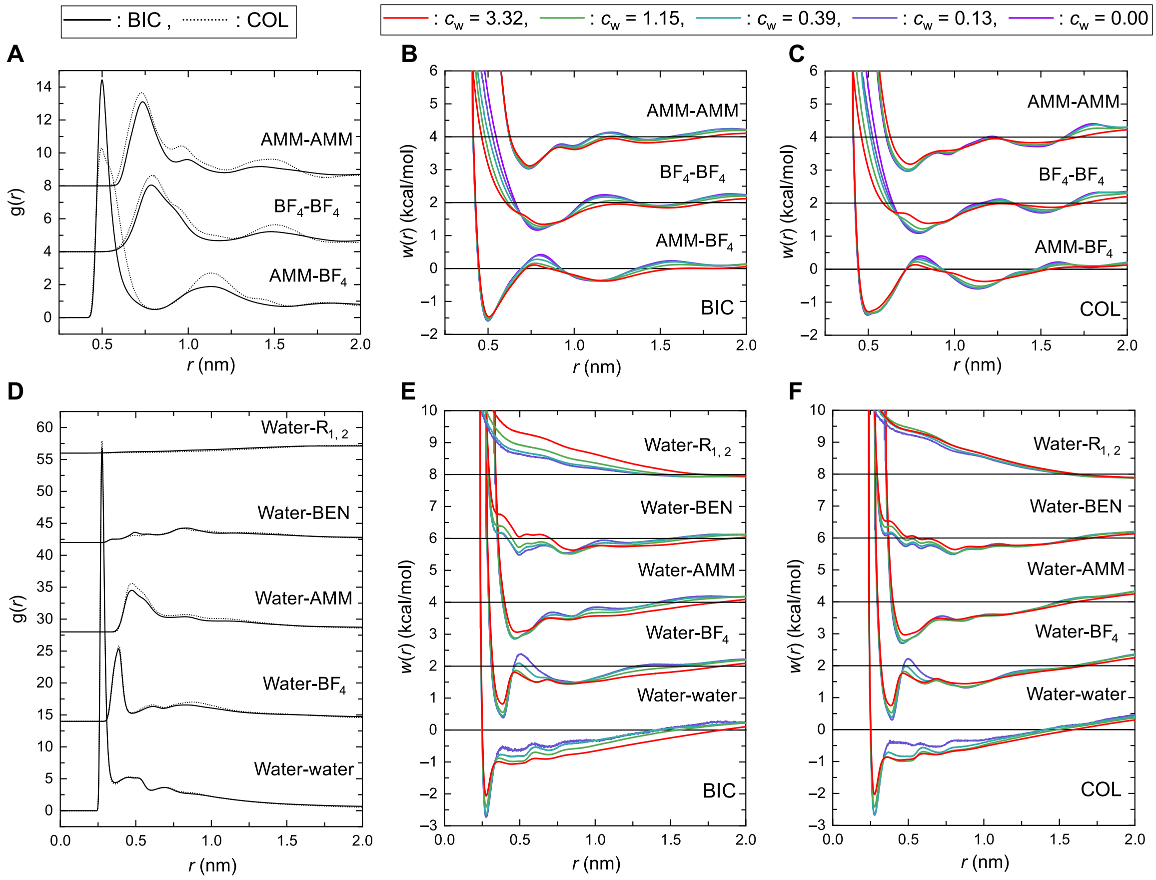

Fig. 3. Short-range structures inside the nanochannels obtained by the MD calculation with OPLS-DFT and TIP3P. (**A** and **D**) Radial distribution functions g(r) and (**B**, **C**, **E**, and **F**) the potentials of mean force $w(r)$. The plots in (B), (C), (E), and (F) are computed in the bicontinuous and columnar structures, respectively. g(r) and $w(r)$ are defined with the pairs of ionic moieties in (A) to (C) and with the pairs of water and anion or atomic groups within the cation in (D) to (F). The referenced position is set to the center of mass of a targeted group, and BEN and AMM refer to the phenyl and ammonium groups, respectively. g(r) and $w(r)$ are shown at c_w = 1.15 M and at all the investigated concentrations, respectively. In the plots of (A) to (C), g(r) is shifted upward by 4 and 8 for BF_4-BF_4 and AMM-AMM, respectively, and $w(r)$ is shifted by 2 and 4. In the plots of (D) to (F), g(r) is shifted upward by 14, 28, 42, and 56 for water-BF_4, water-AMM, water-BEN, and water-$R_{1,2}$, respectively, and $w(r)$ is shifted by 2, 4, 6, and 8. See fig. S15 for the results with OPLS-DFT and TIP4P/2005.

binding free energy of −1.4 to 1.5 kcal/mol. It is stronger than the $-RT = -0.6$ kcal/mol at 300 K. In contrast, the energy barrier between the first and second coordination shells is smaller than the RT, and it further decreases by the addition of water molecules. The potential wells of like ions then become shallower in response to c_w. The first peaks of $w(r)$ between the cation pairs remain fixed with respect to c_w. However, as seen in the shifts of the first minimum given by the anion pairs, BF_4 anions get to contact gradually by the addition of water molecules. Furthermore, as effects of self-assembled nanostructures, we can find that the contact ion pair of unlike ions tends to be tightly bound in the bicontinuous structure, whereas the columnar structure can form the large aggregations of like ions as illustrated with the larger second peaks of g(r).

Figure 3 (D to F) shows the radial distribution functions g(r) and potentials of mean force $w(r)$ given by the pairs of water and anion or atomic groups within the cation. First, water molecules are most strongly bonded in the coordination shell of a water molecule. The binding free energy yields −2.8 to 2.0 kcal/mol, which is more favored than the case of contact ion pair. Water molecules are thereby found to strongly contact inside the nanochannels of compound **1**. In addition, the reduction of an energy gap between the first and second coordination shells indicates the aggregation of water molecules by an increase of c_w. These results suggest the network formation of water molecules confined inside the ionic nanochannel. BF_4 anions secondly contact to a water molecule with the binding free energy of −1.6 to 1.3 kcal/mol. The addition of water molecules decreases the energy barrier between the first and second coordination shells and gives rise to the metastable state at 0.70 to 0.75 nm without any position shifts of the first and second peaks. These behaviors can be interpreted as the cooperative motion of water and BF_4 anions inside the ILC nanochannel when the water pathway enlarged. From the 2D potential of mean force for phenyl group within the cation (figs. S16 and S17), while the phenyl groups of cations are stacked by −1.3 kcal/mol at the low-c_w region, the addition of water molecules reduces the stacking energy. Thereby, we can find that the ILC nanochannels become soft by enlarging the water pathway. Here, we remark that, while the interaction of water molecules is stronger than that of BF_4 anion as reported by McDaniel and co-workers (*22*), the ionic bond between cation and anion remains effective with the coordination number of 3.9 to 3.6 to preserve the 1D and 3D-interconnected nanochannels. For the ammonium group, the potential of mean force is weakly affected by c_w, and the binding free energy is also relatively weak as −1.3 to 0.9 kcal/mol. Water molecules further feel weak attractive interactions of less than −0.5 kcal/mol from the phenyl groups, and the probable distance gets to be shifted toward 0.7 nm or more with an increase of c_w. In contrast, short-range interactions with a water molecule are unfavorable for the alkyl chains of R_1 and R_2, and the columnar structure further amplifies the hydrophobic effect due to the structural contrast of hydrophobic and hydrophilic domains.

Figure 4 shows structural information for the hydrogen bonds of water molecules confined in the ionic nanochannels. The hydrogen bonds are defined with the cutoff length of 0.33 nm by the pairs of water molecules and the groups of ionic moieties. Figure 4A shows the averaged number of hydrogen bonds of a water molecule. An increase of the c_w enhances the formation of hydrogen bonds among water molecules, and the total number of hydrogen bonds yields four at c_w = 3.32 M. Here, we note that the columnar structure slightly amplifies the number of hydrogen bonds with the ionic moieties. We further analyze the size of the hydrogen bonding network. A set of water molecules is defined as forming a hydrogen bonding cluster when a path of hydrogen bonds within the set is present for each pair of water molecules in the set. Figure 4B shows the probability of the number of the hydrogen bonding cluster, and Fig. 4C shows the averaged number of the cluster in an MD system. At c_w = 0.39 M, water clusters are mainly observed to consist of less than 10 molecules. Thereby, as seen in Fig. 4C, the addition of water molecules simply increases the number of hydrogen bonding clusters at the low-c_w region of less than 1 M. On the other hand, at c_w = 3.32 M, the probabilities of small clusters decrease, and large clusters are observed to consist of more than 100 water molecules.

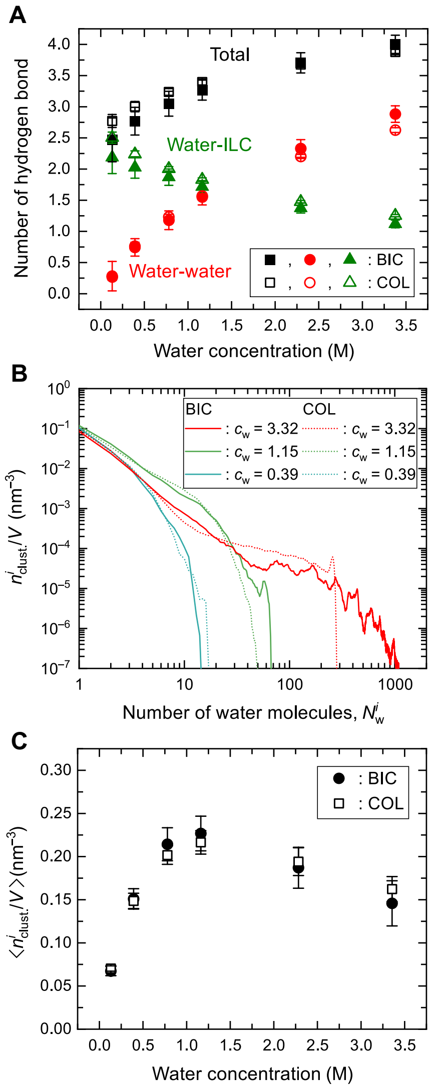

Fig. 4. Hydrogen bonding structures of confined waters in the nanochannels obtained by the MD calculation with OPLS-DFT and TIP3P. (**A**) Averaged numbers of hydrogen bonds of a water molecule with the other water and ionic moieties, (**B**) probability of a hydrogen bonding water cluster, and (**C**) the averaged number of hydrogen-bonded water clusters. $n^i_{clust.}$ is the number of a cluster i in volume V, and N^i_w is the number of water molecule in the cluster i. The probability and averaged number of water clusters are normalized with the system volume V. The summation of its product, $\Sigma_i n^i_{clust.} N^i_w / V$, is equal to the number density of water in an MD cell. See fig. S18 for the results with OPLS-DFT and TIP4P/2005.

As a result, as seen in Fig. 4C, the averaged number of hydrogen bonding cluster decreases at the high-c_w region of more than 1 M. These trends of water molecules can be reproduced with the combination of OPLS-DFT and TIP4P/2005 (fig. S18). Thereby, we can understand that confined waters form the hydrogen bonding network in the preserved 1D and 3D nanochannels of self-assembled structures.

Energetic and transport properties in self-assembled ILC

We then move on to the energetic and transport properties of water molecules in ILC. Here, we consider that an arbitrarily chosen, tagged water molecule is a solute, and the corresponding solvent consists of the other molecules of cation, anion, and water. Figure 5 (A and B) shows a hydrogen bonding state and the solute-solvent potential energy of the tagged water molecule. In this study, the hydrogen bonding states are classified into four patterns: solitary state bonded only to the ionic moieties, interfacial state bonded to both the ionic moieties and water molecules, bulk-like state bonded only to water molecules, and hydrophobic state bonded to the hydrophobic moieties. The solitary state is mainly observed at the low-c_w region with the potential energy of −12.1 to 13.4 kcal/mol. The interfacial state is dominant at the high-c_w region, and the potential energy changes from −15.7 to −17.9 kcal/mol in response to the water concentration. Here, we note that the bulk-like state is less stable than the interfacial state at the low-c_w region. However, as seen in Fig. 5B, the potential energy of bulk-like water strongly depends on c_w, and the energetic trend is remarkably reversed at the high-c_w region of more than 1 M. These results reflect the growth of water clusters depending on the water concentration as observed in Fig. 4C. In all the states, the potential energy of bulk-like state yields the lowest value of −18.8 kcal/mol at c_w = 3.32 M, which is still weaker than that of pure water. The fraction of hydrophobic state is quite small by less than 0.6% with the potential energy of −8.6 to 9.3 kcal/mol regardless of c_w. Thereby, we can understand that water molecules interact favorably with the ionic domain of the nanochannel at the low-c_w region, but with an increase of the water concentration, the formation of hydrogen bonding networks by solvent water molecules allows a tagged water molecule to stay in the water-rich domain of the nanochannel.

Next, we focus on the interactions of water in ILC. The partitioning of water is governed by Δμ, the free-energy change for turning on the interactions of a tagged water molecule with all of the cations, the anions, and the other water molecules. We call Δμ solvation free energy by viewing the tagged water molecules as the solute and the others as the solvent. It is the free energy of transfer of the tagged water from vacuum to the ILC medium and quantifies the extent of stabilization due to the interactions of the solute with the surrounding solvent molecules. The solvation free energy was computed by using the energy representation method in the solution system of interest as follows (*61*–*63*)

$$\Delta\mu = \Delta\mu_{\mathrm{ILC}} + \Delta\mu_{\mathrm{w}} \qquad (1)$$

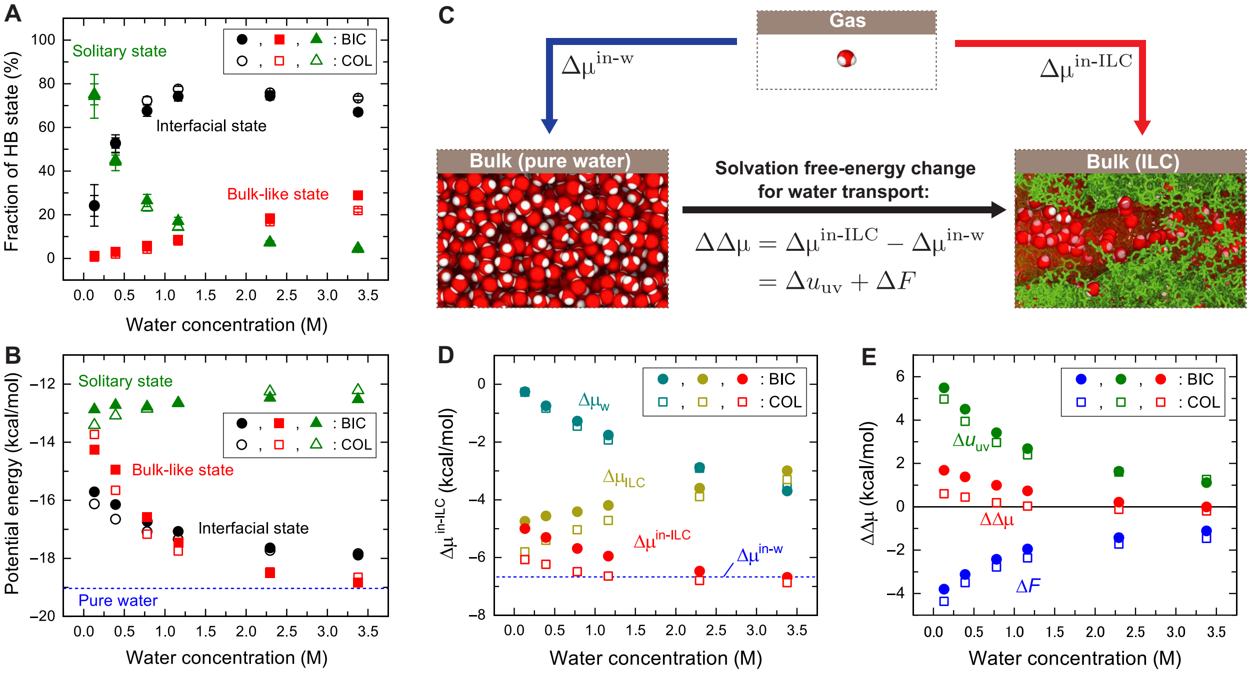

Fig. 5. Hydrogen bonding states and free energetics of confined waters in the nanochannels obtained by the MD calculation with OPLS-DFT and TIP3P. (**A**) Fraction of the hydrogen bonding (HB) state for a tagged water molecule and (**B**) the solute-solvent potential energy in ILC. The hydrogen bonding states are classified as the four patterns of solitary, interfacial, bulk-like, and hydrophobic states. The values for the hydrophobic state are not shown in the figures since they are out of the ranges depicted. See the subsection of "Energetic and transport properties in self-assembled ILC" for the fraction and potential energy at the hydrophobic state. (**C**) An overview of the thermodynamic cycle to compute free-energy change for water transport from pure water to the ILC medium. (**D**) Solvation free energy of water molecule $\Delta\mu^{\text{in-ILC}}$ in ILC and (**E**) the change of solvation free energy ΔΔμ between the media of pure water and ILC. The $\Delta\mu_{\text{ILC}}$ and $\Delta\mu_{\text{w}}$ represent the partial contributions to $\Delta\mu^{\text{in-ILC}}$ from ILC and water molecules, respectively. Δu_{uv} and ΔF mean the differences of solvation energy and solvent-reorganization effect, respectively, between the media of pure water and ILC. Twice the SEs (at 95% confidence interval) of numerical values is smaller than 0.2 kcal/mol. See fig. S19 for the results with OPLS-DFT and TIP4P/2005.

$$= \sum_{i}^{\text{ILC or w}} \int d\varepsilon_i \varepsilon_i \rho_i(\varepsilon_i) + \sum_i \int d\varepsilon_i f(\varepsilon_i) \tag{2}$$

$$= u_{\mathrm{uv}} + F \tag{3}$$

where $\Delta\mu_{\mathrm{ILC}}$ and $\Delta\mu_{\mathrm{w}}$ are the partial contributions from ILC and water molecules, respectively, ε_i is the pair potential energy with the solvent species i, ρ_i (ε_i) is the energetic distribution for ε_i in the solution, and f (ε_i) is a functional taking account of the solvent-reorganization effect including excluded-volume effects; the solvent-reorganization term refers to the free-energy penalty for the structural change of solvent due to the insertion of a solute molecule. The u_{uv} and F terms represent the contributions of solute-solvent interaction and solvent-reorganization effect, respectively.

We consider a thermodynamic cycle to investigate a free-energy change for the water transport process from pure water to the ILC medium. Figure 5C shows the thermodynamic cycle used in this study and the calculated solvation free energy in response to the water concentration. First, according to Fig. 5D, the solvation free energy in ILC $\Delta\mu^{\text{in-ILC}}$ decreases with an increase of c_{w}, and it becomes close to the solvation free energy obtained in pure water $\Delta\mu^{\text{in-w}}$. The stability of a tagged water molecule is thereby found to be comparable between the two media of pure water and ILC at the high-c_{w} region of more than 1 M. Here, the $\Delta\mu^{\text{in-ILC}}$ is decomposed into the partial contributions from water and ILC molecules as $\Delta\mu_{\mathrm{w}}$ and $\Delta\mu_{\mathrm{ILC}}$, respectively. Then, we can understand that while the solvation effect of ionic moieties becomes weakened by the addition of water molecules, the hydration structure formed by solvent water molecules plays an important role to enhance the stability of a tagged water molecule. We further note that, at the low-c_{w} region, the columnar structure has an energetic advantage for the $\Delta\mu^{\text{in-ILC}}$ in comparison with the bicontinuous structure. It reflects the difference of hydrogen bonds with ionic moieties as observed in Fig. 4A. According to the clear contrast of hydrophobic and hydrophilic domains observed in Fig. 3F, the direct interaction with ionic moieties is enhanced in the columnar structure. Thereby, it turns out that the nanochannel formed in columnar structure profits the stability of water molecules.

A solvation free-energy change of the water transport process $\Delta\Delta\mu$ through the interface of pure water and ILC media can be derived via the thermodynamic cycle of Fig. 5C as follows

$$\Delta\Delta\mu = \Delta\mu^{\text{in-ILC}} - \Delta\mu^{\text{in-w}} \tag{4}$$

$$= \Delta u_{\mathrm{uv}} + \Delta F \tag{5}$$

where Δu_{uv} and ΔF are the partial contributions from the differences of solute-solvent interaction and solvent-reorganization effect, respectively, between the media of pure water and ILC. Figure 5E shows the partial contributions of Δu_{uv} and ΔF in response to the water concentration. $\Delta\Delta\mu$ is a few kilocalories per mole at the low-c_{w} region and decreases to zero with an increase of c_{w}. The columnar structure further reduces $\Delta\Delta\mu$ at the low-c_{w} region in comparison with the bicontinuous structure. This difference is provided by the partial contribution from ILC molecules $\Delta\mu_{\mathrm{ILC}}$ as discussed in the preceding paragraph. Hence, we can find that the nanochannels of columnar structure have an energetic advantage for the water transport process between the media of pure water and ILC via the ordering LC structures. Δu_{uv} and ΔF terms exhibit positive and negative values, respectively, over the investigated concentrations. These results suggest that, on the transport process from pure water to the ILC medium, a tagged water molecule feels repulsive and attractive effects by the differences of solute-solvent interaction and solvent-reorganization effect, respectively.

Figure 6 (A and B) shows the self-diffusion coefficients and ionic conductivities in ILC. The transport coefficients are calculated with the mean-square displacements of molecular trajectories by the Einstein equation (figs. S20 to S23). We examine the anisotropy of diffusion coefficient in the columnar structure in Discussion, and here, we focus only on the one averaged over all the directions. In the ILC nanochannels, water molecule diffuses faster than the ammonium-based cation and $\mathrm{BF_4}$ anion, and the self-diffusion coefficient D_{w} is of the order of 10^{-12} to 10^{-10} $\mathrm{m^2/s}$ depending on c_{w}. The low diffusivity is sufficiently reasonable since confined water in electrolytes gives slow mobility as observed in ionic liquids (*25*, *46*) and in the vicinity of rod-like polyelectrolytes (*64*, *65*). The counterion condensation (*32*, *33*) also supports the present results that the ILC nanochannels slow down the dynamics of confined waters due to the existence of condensed and tightly bound counterions via the high ion density of nanochannels (see section S4). In comparison with the various confined environments of CNT, Nafion, and lyotropic ILC (*26*, *27*, *30*, *37*), we can summarize that the order of D_{w} is pure water ~ the CNT nanochannel in 10^{-9} $\mathrm{m^2/s}$ > the Nafion nanochannel in 10^{-10} $\mathrm{m^2/s} \geq$ the ILC nanochannel in 10^{-10} to 10^{-11} $\mathrm{m^2/s}$. For ionic molecules, the mobilities of ammonium-based cation and $\mathrm{BF_4}$ anion are further slow, and the corresponding self-diffusion coefficients of D_{c} and D_{a} are of the order of 10^{-13} to 10^{-12} $\mathrm{m^2/s}$. We note that while $D_{\mathrm{w}}/D_{\mathrm{c}}$ remains unchanged with an increase of c_{w}, $D_{\mathrm{w}}/D_{\mathrm{a}}$ reduces from 72 ($c_{\mathrm{w}} = 0.13$ M) to 15 ($c_{\mathrm{w}} = 3.32$ M) as experimentally reported in the mixtures of 1-decyl-3-methylimidazolium tetrafluoroborate and water (*25*). The addition of water molecules enhances the diffusivity of $\mathrm{BF_4}$ anions, which contributes to an increase of the ionic conductivity. In the columnar structure, the 2D potential of mean force also shows that the $\mathrm{BF_4}$ anions tend to be trapped inside the nanochannel (figs. S16 and S17), while they are released with an increase of c_{w} as mentioned by Nada *et al.* (*35*). We further remark the agreement of ionic conductivity at $c_{\mathrm{w}} = 0.00$ M with the experimental range of 10^{-6} to 10^{-5} S/cm measured for 3,4,5-tri(dodecyloxy)benzyl-triethylammonium trifluoroborate (*17*). These anion mobility and ionic conductivity may relate to ion transport properties of the ILC nanochannels.

DISCUSSION

In the 1D and 3D nanochannels of self-assembled ILC, the interaction of a water molecule becomes strong by forming the hydration shell and hydrogen bonding network, but the potential energy remains smaller than the case of pure water. On the water-dissolution process into the confined environment, the free-energy penalty of structural reorganization expressed as $\Delta F < 0$ due to the insertion of a water molecule plays a key role for the water partitioning by compensating the loss of the interactions of the water molecule with the surroundings. Here, we revisit the understanding of confined waters in room-temperature ionic liquids (*21*–*25*); water molecules are solvated into small cavities among the hydrophilic molecules, and the aggregation of water molecules behaves as a water pocket. These scenarios are consistent with the insight in fig. S11 that the free

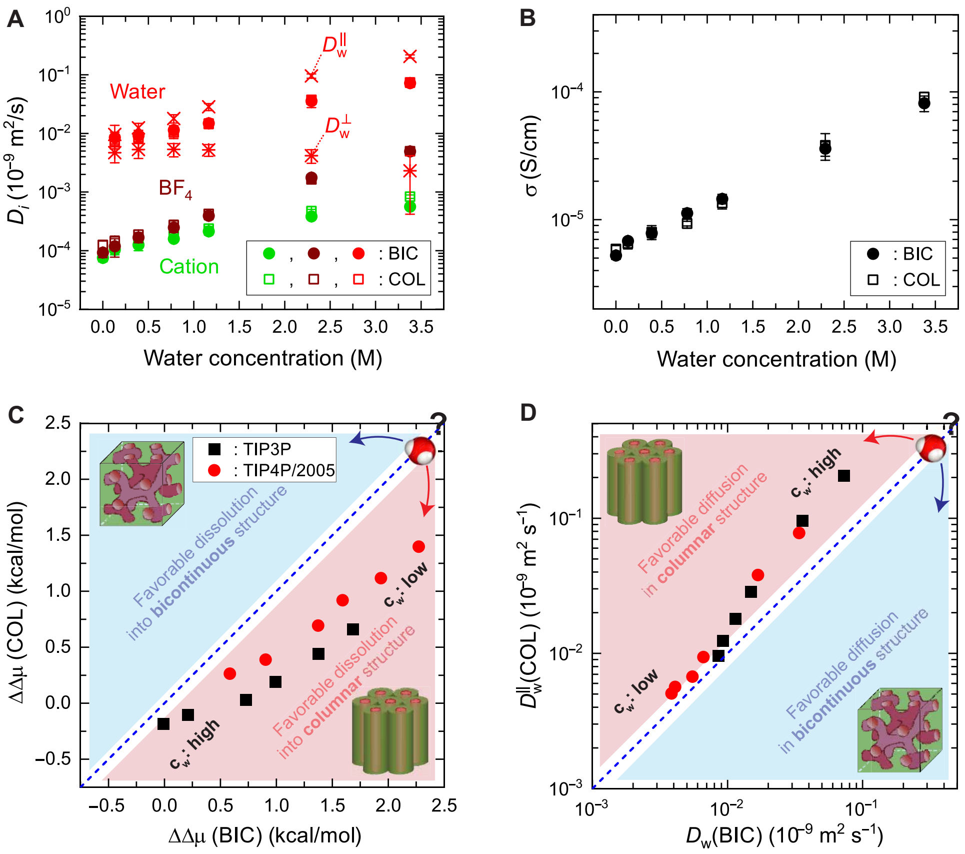

Fig. 6. Transport properties of water and ions obtained by the MD calculation and quantitative comparisons of diffusion and free-energy profiles between the bicontinuous and columnar structures. (**A**) Self-diffusion coefficients of ammonium-based cation, BF$_4$ anion, and water molecules and (**B**) ionic conductivities in the bicontinuous and columnar structures obtained by the MD calculations with OPLS-DFT and TIP3P. $D^{||}_{w,COL}$ and $D^{\perp}_{w,COL}$ are the longitudinal and transverse self-diffusion coefficients, respectively, of water molecules computed in the columnar structure. The longitudinal and transverse diffusions are defined with the *z* axis along the 1D ionic nanochannels and the perpendicular *xy* plane, respectively, as observed in Fig. 2 (E and F). The corresponding data for cation and anion are shown in fig. S23A. The error bars are shown with twice the SEs (at 95% confidence interval). See figs. S22 and S23 for the further results with OPLS-DFT and TIP3P and for the results with OPLS-DFT and TIP4P/2005. Comparisons of (**C**) the solvation free-energy changes, ΔΔμ (BIC) and ΔΔμ (COL), and (**D**) self-diffusion coefficients, D_w(BIC) and $D_w^{||}$(COL), of a water molecule in the bicontinuous and columnar structures, respectively. The red area of ΔΔμ (COL) < ΔΔμ (BIC) and $D_w^{||}$(COL) > D_w(BIC) represents the favorable dissolution-diffusion region in the columnar structure, and oppositely, the blue area of ΔΔμ (COL) > ΔΔμ (BIC) and $D_w^{||}$(COL) < D_w(BIC) represents the favorable dissolution-diffusion region in the bicontinuous structure. The dashed lines are guides to the eye for ΔΔμ (COL) = ΔΔμ (BIC) and $D_w^{||}$(COL) = D_w(BIC).

volume is larger in the ILC than in pure water. The increased free volume is reflected as the reduced free-energy penalty of solvent reorganization expressed and facilitates the water dissolution into the ILC. When increasing the water concentration, the solute-solvent interaction of confined waters reduces inside the nanochannels, and then the Δ*F* advantage becomes weakened because of the formation of hydrogen bonding water networks. Meanwhile, the difference of solvent-reorganization effect remains negative as compensation for the loss of solute-solvent interaction. As a result of the compensation, the confined environment inside the ILC nanochannel is energetically comparable with the pure water at the high-c_w region of 2 M or more.

The hydration effect increases the mobilities of waters and BF$_4$ anions and thus activates the ion conduction in the ILC media. The diffusivity of confined water inside the ILC nanochannel is comparable with the Nafion nanochannel. Here, by using the columnar LC structures, we discuss anisotropic diffusivity of molecules inside the ILC nanochannel. The longitudinal diffusion is defined with the mean-square displacement along the *z* axis parallel to the columnar direction, and the transverse diffusion is thus defined with the mean-square displacement along the *xy* plane perpendicular to the columnar direction (figs. S23 and S24). As seen in Fig. 6A, the longitudinal self-diffusion coefficient of water molecules $D^{||}_w$ is higher than the D_w, and the addition of water molecules enhances the longitudinal mobility up to $D^{||}_w/D_w = 2.55$. On the other hand, the transverse diffusivity $D^{\perp}_w/D_w$ drastically reduces from 0.59 to 0.03 with an increase of c_w. At $c_w = 3.32$ M, $D^{\perp}_w$ is almost equivalent to the self-diffusion coefficient of BF$_4$ anion, but it should be remarked that the transverse mean-square displacements remain anomalous to accurately determine the transverse diffusivity with the observed range of time scale (fig. S24). Nevertheless, the damping of transverse mean-square displacement and the increase of $D^{||}_w/D_w$ clearly support that the transverse diffusion of water molecules slows down with an increase of c_w and then the 1D nanodomain of columnar structure amplifies the longitudinal mobility of confined water by the reduction of transverse motion. The diffusion anisotropies of ammonium-based cation and BF_4 anion seem to be small relatively (fig. S23). These results suggest that the preparation of water pathway inside the nanochannel as hydrogen bonding network activates the anisotropic diffusion of water molecules parallel to the pathway direction. According to the visualization of water trajectories shown in fig. S25, confined waters diffuse in the nanochannels, and the possibility of water transfer event among nanochannels through the hydrophobic domain is quite low because of the high activation energy across nanochannels (fig. S16 and S17). Note that these structural, energetic, and transport properties of confined water are commonly observed with the water models of TIP3P and TIP4P/2005 (sections S2 to S4). We further remark that, since the bicontinuous structure provides high D_w comparable with the columnar structure, the anisotropic mobility of water along the own pathway would be also observed in confined spaces of the bicontinuous one. However, the gyroid-like 3D nanodomain motif is interconnected through all the nanochannels under the periodic boundary condition (fig. S9), which forces to macroscopically cancel out the diffusion anisotropy in the self-assembled ILC. Thereby, it turns out that the 1D columnar structure can achieve the efficient mobility of water molecules confined in the ILC media.

Last, we mention the ability of the ILC medium for water transport. In general, the columnar structure is expected to advantage water transport through the mesoscale geometry of 1D aligned nanodomain, and the bicontinuous structure forming the 3D continuous nanodomain network is valuable from the materials perspective such as the fabrication process and the long-term use against clogging of transport pathway. In water transport process, a water molecule is partitioned into the ILC medium and diffuses in the nanochannels: These behaviors can be quantified by $\Delta\Delta\mu$ and D_w, respectively. Thereby, to elucidate molecular insights on confined water in the ILC nanochannels, we compare the diffusion coefficient and free-energy changes between the self-assembled columnar and bicontinuous structures as shown in Fig. 6 (C and D). First, as seen in Fig. 6C, the columnar structure of compound **1** gives favorable (more negative) $\Delta\Delta\mu$ than the bicontinuous one. The low-c_w region amplifies the $\Delta\Delta\mu$ difference via the partial contribution from ILC molecules, $\Delta\mu_{ILC}$, shown in Fig. 5C. The preparation of water pathway inside the nanochannel weakens the interaction of water and ionic molecules, so that the dissolution advantage of columnar structure disappears by increasing water molecules confined in the ILC nanochannel. However, Fig. 6D shows that, at the high-c_w region, the columnar structure gives favorable (larger) water diffusivity with the orientation of 1D nanochannels. This diffusion advantage depends on the water content forming the hydrogen bonding network in the ILC nanochannel. The intermolecular interactions such as hydrogen bonding are thus shown to be decisive in the permeation inside the nanochannels of ILC membrane as evidenced in Figs. 4 to 6. Therefore, the statistical-mechanical analysis at atomic resolution is of help to prepare a guideline of the competitive interaction of water and ionic nanochannels for imaging the molecular structures of self-assembled ILC membrane. Moreover, hydrogen bonding structures of water molecules in the nanochannels determine the permeation selectivity of inorganic ions such as Na^+ and Mg^{2+} (*11*, *13*), which was revealed by soft x-ray emission spectroscopy (*15*, *66*). The combination of this experimental observation and the computational results in the present study also leads to the design of functional water treatment membranes.

MATERIALS AND METHODS

Chemical structure of the investigated ILC

The chemical structure of ILC compound **1** is depicted in Fig. 1A. The cation involves an ionic moiety of *N*-methyl-*N*,*N*,*N*-triethylammonium group, and the terminals of the two alkyl chains are conjugated dienes. The anion is tetrafluoroborate BF_4. The molecular and atomic group charges of cation and anion of compound **1** are shown in table S1.

Force field

We rely on the OPLS force field (called original OPLS here) with all-atom model refined for long hydrocarbons and ionic liquids (*42*, *57*–*60*). The force-field parameters are cited from the parameter library provided in Gromacs 2016.5 (*67*) as following the OPLS manner (*57*–*60*) and complemented for the lacking ones of ammonium group and BF_4 anion from the additional parameter set by Canongia Lopes *et al.* (*42*). See the section of "Data and materials availability" for the detailed force-field data. The parameter sets of OPLS were well tested for standard organic compounds and ionic liquid materials (*46*–*49*). In this study, the atomic charges were further tuned in condensed phase via the self-consistent scheme combining MD and DFT methods established previously (*47*–*49*). The production MD was performed as described in the subsection of "System setups for the self-assembled ILCs", although the system size used there is too large for DFT calculations. We thus use a smaller system for tuning the force field; see the next subsection for the iterative scheme of MD and DFT.

Computational procedure of the iterative MD/DFT modeling

In the DFT part of self-consistent modeling, we used a linear-scaling DFT calculation with the periodic subnanochannel of compound **1** depicted in Fig. 1C. The initial molecular structure of subnanochannel was prepared by following the early study of similar compounds by Nada *et al.* (*35*). One of the layers consists of four ion pairs. The ammonium groups within the cation are located as a square shape in the monolayer. The distances between the N atoms of the neighboring ammonium groups are set to be 1 nm, which is slightly larger than the distance of Nada *et al.* by taking into consideration the full-atomistic model used in this study (*35*). The BF_4 anions are placed by setting its center of mass at the midpoint of each adjacent pair of N atoms, and the monolayer forms a parallelogram with an angle of 60°. The subnanochannel was constructed as eight layers by stacking the adjacent layers at an angle of 45°: 32 ion pairs (the 4608 atoms) are included in the monoclinic cell. The nearest N-N distance between the layers is 0.7 to 0.8 nm, and the molecular conformation is relaxed through the energy minimization calculation with the steepest descent method. The set of atomic charges was updated by performing the DFT calculations done against the snapshot configurations taken from an MD trajectory, and then an MD calculation was performed with the updated atomic charges to sample a new trajectory. The iterative MD and DFT scheme was repeated four times as demonstrated in the previous study (*49*). The advanced nonpolarizable force field, called OPLS-DFT in the present paper, was used with the combination of TIP3P or TIP4P/2005 model (*56*).

The CP2K package was used for the linear-scaling DFT calculation. The electronic state calculation was carried out in the framework of Gaussian plane wave method (*68*). The Gaussian basis was set to double-ζ valence basis set augmented with a polarization function. The Perdew-Burke-Ernzerhof (PBE) generalized-gradient approximation was used for the exchange-correlation functional. The density cutoff was set to be 400 Ry. The DFT calculations were performed against MD snapshot configurations (described in the next paragraph) and treated the whole set of particles in MD under the periodic boundary condition. The MD snapshots were used without modification such as geometry optimization. The atomic charges Q_{ia} of the site a within molecule i were calculated via the Blöchl fitting procedure for the electron density by using the method of Lagrange multiplier as follows (*69*)

$$F(Q_{ia},\lambda) = \frac{V}{2}\sum_{\boldsymbol{G}\neq 0} w(\boldsymbol{G})\left| n(\boldsymbol{G}) - \sum_i \sum_a Q_{ia} g_{ia}(\boldsymbol{G})\right|^2 - \lambda\left[n(\boldsymbol{G}=0)V - \sum_i \sum_a Q_{ia} g_{ia}(\boldsymbol{G}=0)V\right] \tag{6}$$

where V is the system volume, $\boldsymbol{G}$ is the reciprocal lattice vector, $n(\boldsymbol{G})$ is the electron density in the reciprocal space, and λ is a Lagrange multiplier. $g_{ia}(\boldsymbol{G})$ is the Gaussian function for atom-centered unit charge introduced as

$$g_{ia}(\boldsymbol{G}) = \int d\boldsymbol{r}\, g(\boldsymbol{r}) \exp(-i\boldsymbol{G}\cdot\boldsymbol{r}) \tag{7}$$

$$g_{ia}(\boldsymbol{r}) = \sum_{l=1}^{3} \frac{1}{\{\sqrt{\pi}\, r_{c,l}\}^3} \exp\left[-\left\{\frac{\boldsymbol{r}-\boldsymbol{r}_{ia}}{r_{c,l}}\right\}^2\right] \tag{8}$$

where $r_{c,l}$ is the decay length of the lth function. $w(\boldsymbol{G})$ is a weighting function defined as

$$w(\boldsymbol{G}) = 4\pi \frac{\left|\boldsymbol{G}^2 - G_c^2\right|^2}{\boldsymbol{G}^2 G_c^2} \left(|\boldsymbol{G}| < G_c \text{ and } \boldsymbol{G} \neq 0\right) \tag{9}$$

where G_c is the cutoff length in the reciprocal space. In Eq. 6, the $\boldsymbol{G} = 0$ term is treated separately to account for the condition of charge neutrality of the total system through the Lagrange multiplier. G_c was set to 2.45 Hartree, and the $r_{c,1}$, $r_{c,2}$, and $r_{c,3}$ were 0.265, 0.397, and 0.595 Å, respectively, with a progression factor of 1.5. The DFT charges averaged over 200 configurations and also over equivalent atoms were used as the effective atomic charges of MD force field.

In the MD part of self-consistent modeling, all the calculations were performed by using Gromacs 2016.5 package (*67*). The equations of motion were integrated with the leap-frog algorithm at a time step of 2.0 fs. The Coulomb interaction was calculated by using smooth particle mesh Ewald method with a spline order of 6 and a relative tolerance of 10^{-5}. The real-space cutoff was set to 1.2 nm, and the number of reciprocal-space meshes was 64 in all the x, y, and z directions. The van der Waals interactions were truncated beyond 1.2 nm with a switching function of 1.0 to 1.2 nm. All the covalent bonds were fixed with the LINCS algorithm. After the equilibration for 5 ns under the *NPT* condition with the velocity-rescaling thermostat and Parrinello-Rahman barostat at coupling times of 2.0 ps, the 100-ns production run was performed under the same conditions. In the *NPT* ensemble, the pressure of 1 bar and the compressibility of 4.5×10^{-5} bar^{-1} were used. The obtained 200 configurations with an interval of 0.5 ns were used to perform the DFT calculation in the preceding paragraph and to update the nonpolarizable force field with effective DFT charges.

System setups for the self-assembled ILCs

The system size of the production MD for observing self-assembled nanostructures of compound **1** is listed in table S2. On the whole, the bicontinuous structure was simulated in the *NPT* ensemble with disordered initial configurations prepared by the annealing procedure described below, and the columnar structure was also treated in the *NPT* with ordered initial configurations at room temperature. A system consists of 450 or 1152 ion pairs for the bicontinuous or columnar structures, respectively, as summarized in table S2. The simulation size of 450 ion pairs roughly corresponds with the minimum periodic system of the cubic bicontinuous LC structure (*18*). For the bicontinuous structure, a disordered structure was first produced by randomly locating the cations, anions, and waters in a 20-nm cube. The cubic system with a side of 20 nm is larger than the target cell size, and the equilibration was first performed in the *NVT* ensemble at 800 K for 1 ns. The system was then deformed into the 9-nm cube with the speed of 0.1 nm/ps at 500 K, followed by further equilibration in the *NPT* ensemble of 500 K and 1 bar for 10 ns. For the columnar structure, an ordered structure was first produced by periodically placing the subnanochannel displayed in Fig. 1C. The 3 × 4 × 3 monoclinic supercell of a subnanochannel was transformed into an orthorhombic system under the periodic boundary condition. Water molecules were placed into the central pore of Fig. 1C with the number determined by the compositions of ILCs. The system was then treated at 200 K for 4 ns and further at 250 K for 6 ns, and subsequent equilibration was carried out in the *NPT* ensemble of 300 K and 1 bar for 10 ns.

All the MD simulations at the setups of table S2 were performed by using Gromacs 2016.5 package (*67*). The equations of motion were integrated with the leap-frog algorithm at a time step of 2.0 fs. The Coulomb interaction was calculated by using smooth particle mesh Ewald method with a spline order of 6 and a relative tolerance of 10^{-5}. The real-space cutoff was set to 1.2 nm, and the number of reciprocal-space meshes was 128 and 192 in all the x, y, and z directions, for the systems with 450 and 1152 ion pairs, respectively. The van der Waals interactions were truncated beyond 1.2 nm with a switching function of 1.0 to 1.2 nm. All the covalent bonds including hydrogen atoms were fixed with the LINCS algorithm. In the bicontinuous structure, after the equilibration for 25 ns at 500 K under the *NPT* ensemble of the velocity-rescaling thermostat and the Parrinello-Rahman barostat with coupling times of 2.0 ps, the system was subsequently annealed for 250 ns from 500 to 300 K by reducing the temperature by 20 K every 25 ns. In the columnar structure, the MD system was equilibrated at 300 K for 50 ns under the *NPT* ensemble. The *NPT* conditions commonly use the pressure of 1 bar and the compressibility of 4.5×10^{-5} bar^{-1}. After the above equilibration process, the 50-ns production run was performed under the same *NPT* condition, for the analyses of density, radial distribution functions, structure factors, self-diffusion coefficient, ionic conductivity, and solvation free energy. To improve the statistics, five independent runs were carried out for the bicontinuous and columnar structures by changing the initial configurations at each thermodynamic state.

Analyses of structural, transport, and energetic properties

Radial distribution functions were evaluated with the pairs of atoms, atomic groups, and molecules of cation, anion, and water. The reference site was set to the center of mass of a targeted group. The hydrogen bond of water molecules was evaluated with the definition of donor-acceptor cutoff distance of 0.33 nm. In addition, by using the calculated radial distribution functions of all the atomic pairs, partial and total structure factors were evaluated via the following equations

$$S_{\alpha\beta}(k) = 1 + 4\pi\rho\int_0^\infty dr\, r^2\{g_{\alpha\beta}(r)-1\}\frac{\sin kr}{kr} \tag{10}$$

$$S(k) = \frac{\sum\sum x_\alpha x_\beta f_\alpha(k) f_\beta(k)}{\{\sum x_\alpha f_\alpha(k)\}^2} S_{\alpha\beta}(k) \tag{11}$$

where $S_{\alpha\beta}(k)$ is the partial structure factor between the pair of atomic species α and β in the reciprocal space k, $g_{\alpha\beta}(r)$ is the corresponding radial distribution function in the real space r, and ρ is the number density of an MD system. $S(k)$ represents the total structure factor, x_α the molar fraction of ion species α, and the $f_\alpha(k)$ the cross section of atomic species α in x-ray diffraction measurement.

For transport properties, self-diffusion coefficient D_i of molecule i was calculated with the Einstein equation as follows

$$D_i = \lim_{t\to\infty}\frac{1}{6t}\left\langle |\boldsymbol{r}_i(t)-\boldsymbol{r}_i(0)|^2\right\rangle \tag{12}$$

where $\boldsymbol{r}_i$ is the coordinate for the center of mass of molecule i, and t is the time. The parallel and perpendicular diffusion coefficients, $D^{\|}_i$ and $D^{\perp}_i$, are further evaluated with the Cartesian coordinates of $z_i = \boldsymbol{r}_i \cdot \boldsymbol{u}^z$ and $\boldsymbol{r}_i^{xy} = \boldsymbol{r}_i - z_i\boldsymbol{u}^z$, respectively, as follows

$$D_i^{\|} = \lim_{t\to\infty}\frac{1}{2t}\left\langle |z_i(t)-z_i(0)|^2\right\rangle \tag{13}$$

$$D_i^{\perp} = \lim_{t\to\infty}\frac{1}{4t}\left\langle |\boldsymbol{r}_i^{xy}(t)-\boldsymbol{r}_i^{xy}(0)|^2\right\rangle \tag{14}$$

where $\boldsymbol{u}^z$ is the unit vector in the z direction, and $\boldsymbol{r}^{xy}_i$ is the 2D vector projected onto the xy plane from $\boldsymbol{r}_i$. Ionic conductivity σ was also evaluated via

$$\sigma = \frac{1}{6k_B VT}\lim_{t\to\infty}\frac{d}{dt}\left\langle \left|\sum_i Q_i\{\boldsymbol{r}_i(t)-\boldsymbol{r}_i(0)\}\right|^2\right\rangle \tag{15}$$

where Q_i is the total charge of molecule i, V is the volume of an MD system, k_B is the Boltzmann constant, and T is the absolute temperature.

For energetic properties, solvation free energy of a water molecule Δμ was evaluated with the energy representation method as follows (*61*–*63*)

$$\Delta\mu = \Delta\mu_{\text{ILC}} + \Delta\mu_{\text{w}} \tag{16}$$

$$= \sum_i^{\text{ILC or w}} \int d\varepsilon_i \varepsilon_i \rho_i(\varepsilon_i) + \sum_i \int d\varepsilon_i f(\varepsilon_i) \tag{17}$$

$$= u_{\text{uv}} + F \tag{18}$$

where $\Delta\mu_{\text{ILC}}$ and $\Delta\mu_{\text{w}}$ are the partial contributions from ILC and water molecules, respectively, ε_i is the pair interaction energy between the solute and solvent species i, $\rho_i(\varepsilon_i)$ is the distribution of pair interaction energy ε_i, and $f(\varepsilon_i)$ is a functional describing the excluded-volume and solvent-reorganization effects. The u_{uv} and F terms represent the contributions of solute-solvent interaction and solvent-reorganization effect, respectively. In this study, the solvation free energy of water molecules is investigated in both the bicontinuous and columnar structures with the two combinations of OPLS-DFT and TIP3P and OPLS-DFT and TIP4P/2005. All the free-energy analysis was carried out by using the ERmod 0.3.6 package (*62*, *63*). By also analyzing the solvation free energy in the pure water solvent of TIP3P or TIP4P/2005 model, the solvation free-energy change ΔΔμ can be expressed as follows

$$\Delta\Delta\mu = \Delta\mu^{\text{in-ILC}} - \Delta\mu^{\text{in-w}} \tag{19}$$

$$= \Delta u_{\text{uv}} + \Delta F \tag{20}$$

where ΔΔμ is the solvation free-energy change between the solvents of ILC and pure water, and $\Delta\mu^{\text{in-ILC}}$ and $\Delta\mu^{\text{in-w}}$ are the solvation free energies obtained in the ILC and pure water solvents, respectively. The Δu_{uv} and ΔF represent the partial contributions of ΔΔμ decomposed by the terms of solute-solvent interaction and solvent-reorganization effect, respectively, as follows

$$\Delta u_{\text{uv}} = u_{\text{uv}}^{\text{in-ILC}} - u_{\text{uv}}^{\text{in-w}} \tag{21}$$

$$\Delta F = F^{\text{in-ILC}} - F^{\text{in-w}} \tag{22}$$

where $u_{\text{uv}}{}^{\text{in-ILC}}$ and $u_{\text{uv}}{}^{\text{in-w}}$ are the solute-solvent interaction in the solutions of ILC and pure water, respectively, and $F^{\text{in-ILC}}$ and $F^{\text{in-w}}$ are the solvent-reorganization effect in the solvents of ILC and pure water, respectively.

For the abovementioned free-energy analysis with the energy representation method, two additional kinds of MD were also conducted: the pure solvent (ILC and solvent water molecules) and an isolated water solute in vacuum. The force-field setting was the same with the solution of interest listed in table S2, and an isothermal MD of the isolated solute was performed at 300 K to prepare a set of (intramolecular) configurations. The pure solvent was also simulated in the *NPT* ensemble at 300 K and 1 bar with the periodic boundary condition and minimum image convention. Through the careful equilibration mentioned in the previous subsection, the production runs were performed under the same condition with 50 ns. The 50,000 snapshot configurations with an interval of 1 ps were stored for the free energy calculation with the energy representation method (*61*–*63*). For the isolated water solute in vacuum, a single water molecule was subject to an isothermal MD for 5000 ns. In this simulation, the solute center of mass was fixed at the origin, and the electrostatic potential was treated as its bare form of 1/*r* without cutoff; the other procedures were the same as those for the solution and pure solvent. The solute was inserted as a test particle into the pure-solvent system at random position and orientation, and the insertion was performed without disturbing the solvent configuration after the MD of pure solvent had been performed independently. The number of insertions was 1000 per pure solvent configuration sampled, leading to the generation of 5×10^7 solute-solvent configurations in total. Actually, the MD of the isolated solute was carried out for 5000 ns simply to prepare 5×10^7 intramolecular configurations that were sampled at an interval of 0.1 ps and were used for test particle insertion.

SUPPLEMENTARY MATERIALS

Supplementary material for this article is available at http://advances.sciencemag.org/cgi/content/full/7/31/eabf0669/DC1

REFERENCES AND NOTES

1. T. Kato, M. Yoshio, T. Ichikawa, B. Soberats, H. Ohno, M. Funahashi, Transport of ions and electrons in nanostructured liquid crystals. *Nat. Rev. Mater.* **2**, 17001 (2017).
2. K. Goossens, K. Lava, C. W. Bielawski, K. Binnemans, Ionic liquid crystals: Versatile materials. *Chem. Rev.* **116**, 4643–4807 (2016).
3. M. Mansueto, S. Laschat, "*Ionic liquid crystals*" in *Handbook of Liquid Crystals*, J. W. Goodby, P. J. Collings, T. Kato, C. Tschierske, H. F. Gleeson, P. Raynes, Eds., (Wiley, ed. 2, 2014), vol. 6, pp. 231–280.
4. D. J. Broer, C. M. Bastiaansen, M. G. Debije, A. P. Schenning, Functional organic materials based on polymerized liquid-crystal monomers: Supramolecular hydrogen-bonded systems. *Angew. Chemie Int. Ed. Engl.* **51**, 7102–7109 (2012).
5. D. L. Gin, W. Gu, B. A. Pindzola, W.-J. Zhou, Polymerized lyotropic liquid crystal assemblies for materials applications. *Acc. Chem. Res.* **34**, 973–980 (2001).
6. C. Tschierske, Development of structural complexity by liquid-crystal self-assembly. *Angew. Chemie Int. Ed. Engl.* **52**, 8828–8878 (2013).
7. T. Ichikawa, T. Kato, H. Ohno, Dimension control of ionic liquids. *Chem. Commun.* **55**, 8205–8214 (2019).
8. M. Yoshio, T. Kagata, K. Hoshino, T. Mukai, H. Ohno, T. Kato, One-dimensional ion-conductive polymer films: Alignment and fixation of ionic channels formed by self-organization of polymerizable columnar liquid crystals. *J. Am. Chem. Soc.* **128**, 5570–5577 (2006).
9. T. Kato, From nanostructured liquid crystals to polymer-based electrolytes. *Angew. Chemie Int. Ed. Engl.* **49**, 7847–7848 (2010).
10. D. L. Gin, R. D. Noble, Designing the next generation of chemical separation membranes. *Science* **332**, 674–676 (2011).
11. M. Henmi, K. Nakatsuji, T. Ichikawa, H. Tomioka, T. Sakamoto, M. Yoshio, T. Kato, Self-organized liquid-crystalline nanostructured membranes for water treatment: Selective permeation of ions. *Adv. Mater.* **24**, 2238–2241 (2012).
12. M. Dischinger, J. Rosenblum, R. D. Noble, D. L. Gin, K. G. Linden, Application of a lyotropic liquid crystal nanofiltration membrane for hydraulic fracturing flowback water: Selectivity and implications for treatment. *J. Memb. Sci.* **543**, 319–327 (2017).
13. T. Sakamoto, T. Ogawa, H. Nada, K. Nakatsuji, M. Mitani, B. Soberats, K. Kawata, M. Yoshio, H. Tomioka, T. Sasaki, M. Kimura, M. Henmi, T. Kato, Development of nanostructured water treatment membranes based on thermotropic liquid crystals: Molecular design of sub-nanoporous materials. *Adv. Sci.* **5**, 1700405 (2018).
14. T. Kato, J. Uchida, T. Ichikawa, T. Sakamoto, Functional liquid crystals towards the next generation of materials. *Angew. Chem. Int. Ed.* **57**, 4355–4371 (2018).
15. R. Watanabe, T. Sakamoto, K. Yamazoe, J. Miyawaki, T. Kato, Y. Harada, Ion selectivity of water molecules in subnanoporous liquid-crystalline water-treatment membranes: A structural study of hydrogen bonding. *Angew. Chemie Int. Ed. Engl.* **59**, 23461–23465 (2020).
16. T. Kato, Self-assembly of phase-segregated liquid crystal structures. *Science* **295**, 2414–2418 (2002).
17. T. Ichikawa, M. Yoshio, A. Hamasaki, T. Mukai, H. Ohno, T. Kato, Self-organization of room-temperature ionic liquids exhibiting liquid-crystalline bicontinuous cubic phases: Formation of nano-ion channel networks. *J. Am. Chem. Soc.* **129**, 10662–10663 (2007).
18. T. Ichikawa, M. Yoshio, A. Hamasaki, J. Kagimoto, H. Ohno, T. Kato, 3D interconnected ionic nano-channels formed in polymer films: Self-organization and polymerization of thermotropic bicontinuous cubic liquid crystals. *J. Am. Chem. Soc.* **133**, 2163–2169 (2011).
19. T. Ichikawa, T. Kato, H. Ohno, 3D continuous water nanosheet as a gyroid minimal surface formed by bicontinuous cubic liquid-crystalline zwitterions. *J. Am. Chem. Soc.* **134**, 11354–11357 (2012).
20. R. Hayes, G. G. Warr, R. Atkin, Structure and nanostructure in ionic liquids. *Chem. Rev.* **115**, 6357–6426 (2015).
21. Y.-L. Wang, S. Sarman, L. Kloo, O. N. Antzutkin, S. Glavatskih, A. Laaksonen, Solvation structures of water in trihexyltetradecylphosphonium-orthoborate ionic liquids. *J. Chem. Phys.* **145**, 064507 (2016).
22. A. Verma, J. P. Stoppelman, J. G. McDaniel, Tuning water networks via ionic liquid/water mixtures. *Int. J. Mol. Sci.* **21**, 403 (2020).
23. H. Abe, T. Takekiyo, M. Shigemi, Y. Yoshimura, S. Tsuge, T. Hanasaki, K. Ohishi, S. Takata, J. Suzuki, Direct evidence of confined water in room-temperature ionic liquids by complementary use of small-angle x-ray and neutron scattering. *J. Phys. Chem. Lett.* **5**, 1175–1180 (2014).
24. K. Saihara, Y. Yoshimura, S. Ohta, A. Shimizu, Properties of water confined in ionic liquids. *Sci. Rep.* **5**, 10619 (2015).
25. K. Kaneko, K. Saihara, Y. Masuda, Y. Yoshimura, A. Shimizu, Dynamic properties of water molecules in ionic liquid/water mixture with various alkyl chain length. *J. Mol. Liq.* **264**, 337–342 (2018).
26. A. Alexiadis, S. Kassinos, Molecular simulation of water in carbon nanotubes. *Chem. Rev.* **108**, 5014–5034 (2008).
27. G. Hummer, J. C. Rasaiah, J. P. Noworyta, Water conduction through the hydrophobic channel of a carbon nanotube. *Nature* **414**, 188–190 (2001).
28. K. Koga, G. T. Gao, H. Tanaka, X. C. Zeng, Formation of ordered ice nanotubes inside carbon nanotubes. *Nature* **412**, 802–805 (2001).
29. S. Yamamoto, S. Hyodo, A computer simulation study of the mesoscopic structure of the polyelectrolyte membrane Nafion. *Polym. J.* **35**, 519–527 (2003).
30. S. Cui, J. Liu, M. E. Selvan, D. J. Keffer, B. J. Edwards, W. V. Steele, A molecular dynamics study of a Nafion polyelectrolyte membrane and the aqueous phase structure for proton transport. *J. Phys. Chem. B* **111**, 2208–2218 (2007).
31. Y. Li, Z. Li, F. Aydin, J. Quan, X. Chen, Y. C. Yao, C. Zhan, Y. Chen, T. A. Pham, A. Noy, Water-ion permselectivity of narrow-diameter carbon nanotubes. *Sci. Adv.* **6**, eaba9966 (2020).
32. G. S. Manning, Limiting laws and counterion condensation in polyelectrolyte solutions i. colligative properties. *J. Chem. Phys.* **51**, 924–933 (1969).
33. F. Oosawa, *Polyelectrolytes* (Marcel Dekker, 1971).
34. H. Yoshida, H. Mizuno, T. Kinjo, H. Washizu, J.-L. Barrat, Molecular dynamics simulation of electrokinetic flow of an aqueous electrolyte solution in nanochannels. *J. Chem. Phys.* **140**, 214701 (2014).
35. H. Nada, T. Sakamoto, M. Henmi, T. Ogawa, M. Kimura, T. Kato, Transport mechanisms of water molecules and ions in sub-nano channels of nanostructured water treatment liquid-crystalline membranes: A molecular dynamics simulation study. *Environ. Sci. Water Res. Technol.* **6**, 604–611 (2020).
36. B. J. Coscia, J. Yelk, M. A. Glaser, D. L. Gin, X. Feng, M. R. Shirts, Understanding the nanoscale structure of inverted hexagonal phase lyotropic liquid crystal polymer membranes. *J. Phys. Chem. B* **123**, 289–309 (2019).
37. B. J. Coscia, M. R. Shirts, Chemically selective transport in a cross-linked H_{II} phase lyotropic liquid crystal membrane. *J. Phys. Chem. B* **123**, 6314–6330 (2019).
38. B. J. Coscia, C. P. Calderon, M. R. Shirts, Statistical inference of transport mechanisms and long time scale behavior from time series of solute trajectories in nanostructured membranes. *J. Phys. Chem. B* **124**, 8110–8123 (2020).
39. M. P. Allen, Molecular simulation of liquid crystals. *Mol. Phys.* **117**, 2391–2417 (2019).
40. G. Saielli, A. Bagno, Y. Wang, Insights on the isotropic-to-Smectic a transition in ionic liquid crystals from coarse-grained molecular dynamics simulations: The role of microphase segregation. *J. Phys. Chem. B* **119**, 3829–3836 (2015).
41. H. Peng, M. Kubo, H. Shiba, Molecular dynamics study of mesophase transitions upon annealing of imidazolium-based ionic liquids with long-alkyl chains. *Phys. Chem. Chem. Phys.* **20**, 9796–9805 (2018).
42. J. N. Canongia Lopes, A. A. H. Pádua, K. Shimizu, Molecular force field for ionic liquids IV: Trialkylimidazolium and alkoxycarbonyl-imidazolium cations; alkylsulfonate and alkylsulfate anions. *J. Phys. Chem. B* **112**, 5039–5046 (2008).
43. Y. Zhang, E. J. Maginn, A simple AIMD approach to derive atomic charges for condensed phase simulation of ionic liquids. *J. Phys. Chem. B* **116**, 10036–10048 (2012).
44. E. Choi, J. G. Mcdaniel, J. R. Schmidt, A. Yethiraj, First-principles, physically motivated force field for the ionic liquid [BMIM][BF$_4$]. *J. Phys. Chem. Lett.* **5**, 2670–2674 (2014).
45. D. Bedrov, J.-P. Piquemal, O. Borodin, A. D. MacKerell Jr., B. Roux, C. Schröder, Molecular dynamics simulations of ionic liquids and electrolytes using polarizable force fields. *Chem. Rev.* **119**, 7940–7995 (2019).
46. Z. Li, R. Bouchal, T. Mendez-Morales, A.-L. Rollet, C. Rizzi, S. Le Vot, F. Favier, B. Rotenberg, O. Borodin, O. Fontaine, M. Salanne, Transport properties of Li-TFSI water-in-salt electrolytes. *J. Phys. Chem. B* **123**, 10514–10521 (2019).
47. R. Ishizuka, N. Matubayasi, Self-consistent determination of atomic charges of ionic liquid through a combination of molecular dynamics simulation and density functional theory. *J. Chem. Theory Comput.* **12**, 804–811 (2016).
48. R. Ishizuka, N. Matubayasi, Effective charges of ionic liquid determined self-consistently through combination of molecular dynamics simulation and density-functional theory. *J. Comput. Chem.* **38**, 2559–2569 (2017).
49. Y. Ishii, N. Matubayasi, Self-consistent scheme combining MD and Order-*N* DFT methods: An improved set of nonpolarizable force fields for ionic liquids. *J. Chem. Theory Comput.* **16**, 651–665 (2020).
50. H. Toriumi, M. Yoshida, M. Mikami, M. Takeuchi, A. Mochizuki, Computer simulation of an antiferroelectric liquid crystalline molecule: The origin of bent structure formation and the molecular packing property of MHPOBC in crystalline phase. *J. Phys. Chem.* **100**, 15207–15210 (1996).
51. M. Yoneya, E. Nishikawa, H. Yokoyama, Searching for nanostructures of the cubic mesophase of liquid crystal molecules, BABH8. *J. Chem. Phys.* **120**, 3699–3705 (2004).
52. M. L. Klein, W. Shinoda, Large-scale molecular dynamics simulations of self-assembling systems. *Science* **321**, 798–800 (2008).
53. G. Tiberio, L. Muccioli, R. Berardi, C. Zannoni, Towards in silico liquid crystals. Realistic transition temperatures and physical properties for n-cyanobiphenyls via molecular dynamics simulations. *ChemPhysChem* **10**, 125–136 (2009).
54. K. Takeda, Y. Andoh, W. Shinoda, S. Okazaki, Structure of hydrated crystal (L_c), tilted gel ($L_{\beta'}$), and liquid crystal (L_α) phases of linear alkylbenzene sulfonate (LAS) studied by X-ray diffraction and molecular dynamics simulation. *Langmuir* **35**, 9011–9019 (2019).

55. G. Watanabe, H. Watanabe, K. Suzuki, H. Yuge, S. Yoshida, T. Mandai, S. Yoneda, H. Sato, M. Hara, J. Yoshida, Visualizing the helical stacking of octahedral metallomesogens with a chiral core. *Chem. Commun.* **56**, 12134–12137 (2020).
56. J. L. F. Abascal, C. Vega, A general purpose model for the condensed phases of water: TIP4P/2005. *J. Chem. Phys.* **123**, 234505 (2005).
57. W. L. Jorgensen, D. L. Severance, Aromatic-aromatic interactions: Free energy profiles for the benzene dimer in water, chloroform, and liquid benzene. *J. Am. Chem. Soc.* **112**, 4768–4774 (1990).
58. W. L. Jorgensen, D. S. Maxwell, J. Tirado-Rives, Development and testing of the OPLS all-atom force field, on conformational energetics and properties of organic liquids. *J. Am. Chem. Soc.* **118**, 11225–11236 (1996).
59. M. L. P. Price, D. Ostrovsky, W. L. Jorgensen, Gas-phase and liquid-state properties of esters, nitriles, and nitro compounds with the OPLS-AA force field. *J. Comput. Chem.* **22**, 1340–1352 (2001).
60. S. W. I. Siu, K. Pluhackova, R. A. Böckmann, Optimization of the OPLS-AA force field for long hydrocarbons. *J. Chem. Theory Comp.* **8**, 1459–1470 (2012).
61. N. Matubayasi, M. Nakahara, Theory of solutions in the energy representation. II. Functional for the chemical potential. *J. Chem. Phys.* **117**, 3605–3616 (2002).
62. S. Sakuraba, N. Matubayasi, ERmod: Fast and versatile computation software for solvation free energy with approximate theory of solutions. *J. Comput. Chem.* **35**, 1592–1608 (2014).
63. N. Matubayasi, Energy-representation theory of solutions: Its formulation and application to soft, molecular aggregates. *Bull. Chem. Soc. Jpn.* **92**, 1910–1927 (2019).
64. H. Washizu, K. Kikuchi, Electric polarizability of DNA in aqueous salt solution. *J. Phys. Chem. B* **110**, 2855–2861 (2006).
65. M. A. F. dos Santos, M. A. Habitzreuter, M. H. Schwade, R. Borrasca, M. Antonacci, G. K. Gonzatti, P. A. Netz, M. C. Barbosa, Dynamical aspects of supercooled TIP3P-water in the grooves of DNA. *J. Chem. Phys.* **150**, 235101 (2019).
66. G. Graziano, Hydrogen-bond filtration. *Nat. Rev. Chem.* **4**, 636 (2020).
67. M. J. Abraham, T. Murtola, R. Schulz, S. Páll, J. C. Smith, B. Hess, E. Lindahl, GROMACS: High performance molecular simulations through multi-level parallelism from laptops to supercomputers. *SoftwareX* **1-2**, 19–25 (2015).
68. J. Vandevondele, M. Krack, F. Mohamed, M. Parrinello, T. Chassaing, J. Hutter, QUICKSTEP: Fast and accurate density functional calculations using a mixed gaussian and plane waves approach. *Comp. Phys. Comm.* **167**, 103–128 (2005).
69. P. E. Blöchl, Electrostatic decoupling of periodic images of plane-wave-expanded densities and derived atomic point charges. *J. Chem. Phys.* **103**, 7422–7428 (1995).
70. A. Stukowski, Visualization and analysis of atomistic simulation data with OVITO-the open visualization tool. *Model. Simul. Mater. Sci. Eng.* **18**, 015012 (2010).

Acknowledgments: The MD and DFT calculations were performed by using the supercomputers of Hokkaido University (Grand Chariot), Research Center for Computational Science at Okazaki, Osaka University (OCTOPUS), and Kyushu University (ITO) partially through the HPCI System Research Project (project IDs: hp200043, hp200055, hp200065, and hp200120). **Funding:** This work is supported by JSPS KAKENHI numbers JP19H05715, JP19H05718, JP20H02058, and JP20K15108 from the Japan Society for the Promotion of Science and by the Elements Strategy Initiative for Catalysts and Batteries number JPMXP0112101003. **Author contributions:** Y.I., T.K., and H.W. designed the research; Y.I., N.M., and H.W. performed all the simulations; Y.I., N.M., G.W., T.K., and H.W. analyzed data; Y.I., N.M., G.W., T.K., and H.W. discussed the results; Y.I., N.M., T.K., and H.W. wrote the paper; G.W. commented on the paper; T.K. and H.W. directed the project supervisions. **Competing interests:** The authors declare that they have no competing interests. **Data and materials availability:** All data needed to evaluate the conclusions in the paper are present in the paper and/or the Supplementary Materials. The force field of OPLS-DFT for compound **1** and the setup files for MD are available as Supplementary Materials (data S1). The force-field files of itp and top formats and the general MD and configuration files of mdp and gro formats are included in data S1 for the isolated structure of cation and anion and condensed structures in the bicontinuous and columnar structures at $c_w = 1.15$ M. Additional data needed to evaluate the conclusions for the configuration, trajectory, and general MD files of every composition and model in this study are available via Zenodo: https://doi.org/10.5281/zenodo.4802590. The codes of DFT and MD calculations and free-energy analysis are CP2K 6.1-branch version, Gromacs 2016.5 version, and ERmod 0.3.6 version, respectively, which are freely available under the GPL license. These packages are used in this study without any modifications. The results of simulations are visualized with OVITO-Pro 3.2.1 version.

Submitted 6 October 2020
Accepted 16 June 2021
Published 28 July 2021
10.1126/sciadv.abf0669

Citation: Y. Ishii, N. Matubayasi, G. Watanabe, T. Kato, H. Washizu, Molecular insights on confined water in the nanochannels of self-assembled ionic liquid crystal. *Sci. Adv.* **7**, eabf0669 (2021).